Michigan Tech Publications

10-3-2022

Carbonate-superstructured solid fuel cells with hydrocarbon fuels

Hanrui Su
Michigan Technological University, hanruis@mtu.edu

Wei Zhang
Michigan Technological University, wzhang5@mtu.edu

Yun Hang Hu
Michigan Technological University, yunhangh@mtu.edu

Follow this and additional works at: https://digitalcommons.mtu.edu/michigantech-p

Part of the Materials Science and Engineering Commons

Recommended Citation

Follow this and additional works at: https://digitalcommons.mtu.edu/michigantech-p
Part of the Materials Science and Engineering Commons

Carbonate-superstructured solid fuel cells with hydrocarbon fuels

Hanrui Su[a], Wei Zhang[a], and Yun Hang Hu[a,1]

A basic requirement for solid oxide fuel cells (SOFCs) is the sintering of electrolyte into a dense impermeable membrane to prevent the mixing of fuel and oxygen for a sufficiently high open-circuit voltage (OCV). However, herein, we demonstrate a different type of fuel cell, a carbonate-superstructured solid fuel cell (CSSFC), in which in situ generation of superstructured carbonate in the porous samarium-doped ceria layer creates a unique electrolyte with ultrahigh ionic conductivity of 0.17 S·cm^{-1} at 550 °C. The CSSFC achieves unprecedented high OCVs (1.051 V at 500 °C and 1.041 V at 550 °C) with methane fuel. Furthermore, the CSSFC exhibits a high peak power density of 215 mW·cm^{-2} with dry methane fuel at 550 °C, which is higher than all reported values of electrolyte-supported SOFCs. This provides a different approach for the development of efficient solid fuel cells.

superstructured solid fuel cell | methane | lithium carbonate

Hydrogen is generally used as a fuel for fuel cells. However, hydrogen must be produced from hydrogen-containing compounds (mainly methane) via an expensive process (1, 2). Therefore, it is highly desirable to develop efficient fuel cells that can directly use hydrocarbon fuels (particularly methane). Solid oxide fuel cells (SOFCs), which are attractive energy conversion systems due to their high energy efficiency and fuel flexibilities, require a high operating temperature (1, 2). Lowering the operating temperature of SOFCs is a central goal for reducing system costs/complexity and enhancing the long-term durability (3–6). However, low-temperature SOFCs (LT-SOFCs) with hydrocarbon fuels suffer from polarization losses caused by temperature drop and carbon deposition (coking). This happens because 1) the hydrocarbon oxidation kinetics are extremely sluggish at lower temperatures due to the strong C–H bonds and 2) carbon deposition deactivates electrodes by covering catalytic sites. However, direct electrochemical oxidation of hydrocarbon via oxygen flux through the electrolyte to the triple-phase boundary (TPB) region can produce more CO_2 and H_2O according to Eq. **1**. These products can facilitate the thermochemical reforming reactions of hydrocarbons at lower temperatures (7). If the O^{2-} flux from the electrolyte is faster (Eq. **2**), carbon deposition can also be removed from the anode, shifting the reaction equilibrium toward CO_2 (8). Therefore, one of the key strategies to improve hydrocarbon oxidation and reduce coking for LT-SOFCs is to increase the oxygen ionic conductivity of electrolytes:

$$C_nH_{2n+2} + (3n + 1)O^{2-} \rightarrow nCO_2 + (n + 1)H_2O + (6n + 2)e^- \qquad [1]$$

$$C + 2O^{2-} \rightarrow CO_2 + 4e^-. \qquad [2]$$
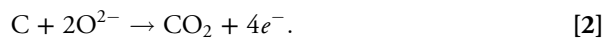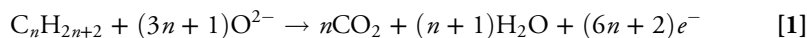
There exist two conventional strategies to enhance the oxygen ionic conductivity of electrolytes in LT-SOFCs, namely, reducing electrolyte thickness and developing fast ionic conductors (3, 4). The ultrathin electrolyte film requires advanced techniques and inevitably increases fabrication cost and complexity. Although bismuth oxides exhibited impressive oxygen ionic conductivity due to their rich oxygen vacancies (4), their poor stability under SOFC operation conditions would hinder their applications. Therefore, other strategies are required to develop efficient ionic conductors.

The unique properties of oxide–carbonate composites have attracted intensive attention (9–11). For yttria-stabilized-zirconia–LiKCO$_3$ composites, density functional theory calculations revealed that the oxygen ionic transfer energy barrier via a cogwheel mechanism at the oxide–carbonate interface was significantly lower than that of bulk conductivity via a direct hopping mechanism (10). Higher oxygen ion conduction was obtained at the interface of the cathode and carbonate via a space-charge layer, thus expanding the TPB (10, 11). The Li doping also promotes the surface oxygen diffusion and further enhances

Significance

Solid oxide fuel cells (SOFCs) are a promising energy conversion system due to their high energy efficiency and fuel flexibility. Lowering the operating temperature of SOFCs can minimize material degradation and enable the use of less expensive materials. However, both electrolyte and electrode resistances increase exponentially with decreasing operation temperature. This work demonstrates a carbonate-superstructured solid fuel cell (CSSFC) by in situ generating superstructured carbonate on the surface of porous electrolyte and the interface between electrodes and electrolyte, dramatically enhancing the oxygen ion conductivity and power density with hydrocarbon fuels at lower operating temperatures.

Author affiliations: ^{a}Department of Materials Science and Engineering, Michigan Technological University, Houghton, MI 49931-1295

^{1}To whom correspondence may be addressed. Email: yunhangh@mtu.edu.

the overall cathode performance (12). These observations stimulated us to form a hypothesis: A continuous interface between molten carbonate and solid ionic conductor can constitute a fast transfer channel for oxygen ions; namely, such a carbonate superstructure on solid ionic conductor would be an oxygen ionic superconductor. To test this hypothesis, we fabricated a device by integrating a $LiNi_{0.8}Co_{0.15}Al_{0.05}O_2$ (NCAL) cathode, a porous $Ce_{0.8}Sm_{0.2}O_{1.9}$ (SDC) electrolyte, and a $Ni-BaZr_{0.1}Ce_{0.7}Y_{0.1}Yb_{0.1}O_{3-\delta}$ (BZCYYb) anode using a one-step dry-pressing procedure without high-temperature sintering in this work. The electrodes and the electrolyte remain porous and nanocrystalline structures in the system. Then, molten carbonate in the porous NCAL and SDC layers is in situ generated at cell operation conditions, creating the carbonate-superstructured fuel cell (CSSFC). Furthermore, the CSSFC exhibited ultrahigh ionic conductivity of 0.17 $S \cdot cm^{-1}$ at 550 °C, leading to an unprecedented high open-circuit voltage (OCV) and a very high peak power density (PPD) as well as excellent coking resistance with dry methane fuel at 550 °C.

Results and Discussion

Fig. 1A illustrates the schematics of conventional SOFCs, SOFCs with porous electrolytes, and CSSFCs. In a conventional SOFC, the oxygen ions are conducted via oxygen vacancies in the bulk crystal structure of electrolyte. A higher sintering temperature is required to increase the grain size for reducing grain-boundary resistance. Moreover, the poor bonding and a limited contact area at the cathode–electrolyte interface would cause large contact/polarization resistance. In contrast, if the molten carbonate is introduced into the porous electrolyte, it would not only enhance the oxygen ion conduction via a continuous interface between molten carbonate and solid ionic conductor but

also build a strong connection in the vicinity of an electrode–electrolyte interface. To verify this, we fabricated several types of SOFCs with Ni-BZCYYb anode, SDC electrolyte, and $(La_{0.60}Sr_{0.40})_{0.95}Co_{0.20}Fe_{0.80}O_{3-\delta}$ (LSCF) cathode. *SI Appendix,* Fig. S1 *A and B* shows the magnified images of the electrolyte layer of porous and dense SDC layers. The porous electrolyte maintained the grain size of the nanocrystalline SDC precursors, along with well-connected open channels, enabling gas diffusion and permeation thoroughgoing. However, a typical polycrystalline SDC with a polygonal grain size larger than 2 μm as well as clear and long boundaries was observed in dense SDC layers owing to the high-temperature sintering process. The total Brunauer–Emmett–Teller (BET) specific surface area of SDC powder or the SDC porous pellet without sintering determined by N_2 adsorption is ~6.0 $m^2 \cdot g^{-1}$ with a typical type IV isotherm and an H3 hysteresis loop (*SI Appendix,* Fig. S2). The electrochemical performance of the conventional SOFC with sintered electrolytes, SOFC with porous electrolytes, and SOFC with carbonate modifications are displayed in Fig. 1B. The cell with 15 wt% Li_2CO_3 added into LSCF cathode exhibited a PPD of about 150 $mW \cdot cm^{-2}$ at 550 °C with dry CH_4 fuel, which is about seven times higher than a conventional SOFC with a dense electrolyte layer (~20 $mW \cdot cm^{-2}$ at 550 °C). The poor performance of the conventional SOFC could be attributed to the ohmic loss of the thick densified SDC electrolyte (~500 μm). Moreover, the cell based on a porous SDC electrolyte layer without carbonate modification generated a very small OCV of 171 mV due to the gas leakage through the porous electrolyte layer. Notably, the enhanced performance by molten Li_2CO_3 for the cell is due to the increase of O_2^- transfer, which is totally different from a typical molten carbonate fuel cell (with a CO_2 flow into its cathode) whose conducting species are CO_3^{2-}. This can be explained as follows: A CO_2 flow, which is

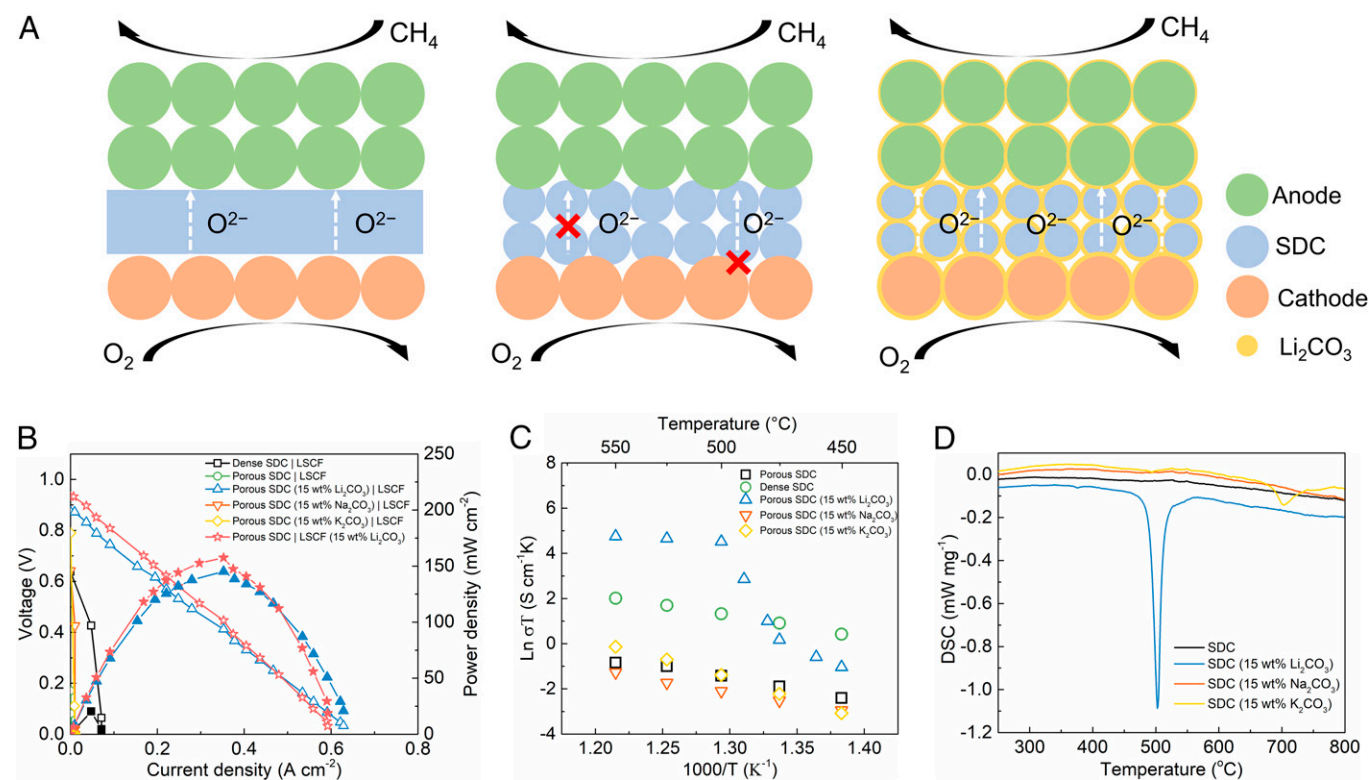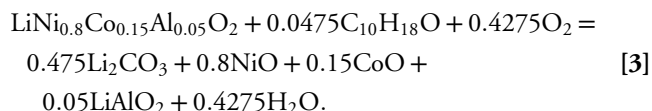**Fig. 1.** (A) Schematic of the conventional SOFC, porous SOFC, and the CSSFC. (B) The I-V-P performance of different fuel cell configurations with Ni-BZCYYb as anodes operated on CH_4 at 550 °C. (C) The temperature-dependent Arrhenius plot of oxygen ionic conductivities of different electrolytes with or without carbonate modification. (D) DSC plots of different electrolytes in Ar atmosphere.

necessary for a typical molten carbonate fuel cell to continuously produce CO_3^{2-} via a cathode half-reaction ($1/2\ O_2 + CO_2 + e^- \leftrightarrow CO_3^{2-}$), was not provided for our cell operation. Therefore, the stable performance of the cell without CO_2 flow demonstrates O_2^- (instead of CO_3^{2-}) transfer in its electrolyte.

The ionic conductivities of SDC and SDC–carbonate composites were also evaluated by measuring the pellet-like samples with painted silver electrodes in dry air atmosphere ($P_{O_2} = 0.21$ atm). As shown in Fig. 1C, the SDC with Li_2CO_3 modification delivers a remarkably high ionic conductivity of 0.14 S·cm^{-1} at 550 °C in air, which is approximately two magnitudes higher than those of densified SDC pellet (9.1×10^{-3} S·cm^{-1}) and porous SDC layer (5.2×10^{-4} S·cm^{-1}). However, the SDC with Na_2CO_3 or K_2CO_3 carbonate showed similar conductivity to that without carbonates. Furthermore, a significant transition temperature (~500 °C) was found in the SDC-Li_2CO_3 composite. Its ionic conductivity decreases sharply by about five times from 500 °C to 490 °C. As shown in the differential scanning calorimetry (DSC) plots (Fig. 1D), a strong endothermic peak appears at 502 °C for the SDC-Li_2CO_3 composite, while no peak was found for pure SDC, SDC-Na_2CO_3, and SDC-K_2CO_3 at the temperature below 600 °C. The transition at 502 °C is attributed to the melting of Li_2CO_3 of the SDC-Li_2CO_3. Although the normal melting temperature of Li_2CO_3 is 723 °C (13), its Tammann temperature is about 400 °C (i.e., it is empirically half its melting temperature), at which its molecules have a remarkable mobility (14). Therefore, Li_2CO_3 molecules can rapidly move to the SDC surface to form a melted Li_2CO_3 layer at 502 °C (probably via the eutectic-phase formation), which is responsible for the ionic conductivity enhancement. For porous SDC, the oxygen ion conduction via oxygen vacancies in the bulk crystal structure of the electrolyte would be inhibited by high grain-boundary resistance. The molten carbonate can build a strong connection at the vicinity of the SDC interface via pore filling, topology change, or contact angle adjustment; reduce the grain-boundary resistance; and increase the interfacial ionic conduction.

Several cathode materials were subjected to the characterization of electrochemical impedance spectroscopy (EIS) under open-circuit conditions from 450 to 550 °C in the air (Fig. 2A). It was found that the Li_2CO_3 modification greatly reduced the polarization area-specific resistance (ASR) of the LSCF electrode from 88.9 to 3.09 Ω·cm^2 at 550 °C, suggesting the promotion effect of Li_2CO_3 on the cathode. To fully demonstrate the role of carbonate in the cathode, a Li-based single-phase cathode, NCAL, was used to replace the mechanically mixed LSCF/Li_2CO_3 composite cathode. The NCAL is a good candidate for a porous cathode material due to its high ionic and electrical conductivities and high oxygen reduction reaction activity (15, 16). Most importantly, the Li_2CO_3 can be in situ generated under fuel cell operation because NCAL can react with the terpineol binder (Eq. 3):

$$LiNi_{0.8}Co_{0.15}Al_{0.05}O_2 + 0.0475C_{10}H_{18}O + 0.4275O_2 =$$
$$0.475Li_2CO_3 + 0.8NiO + 0.15CoO + \qquad \textbf{[3]}$$
$$0.05LiAlO_2 + 0.4275H_2O.$$

Indeed, the Fourier-transform infrared spectroscopy (FTIR) spectra show the characteristic peaks of Li_2CO_3 at ~1,500 cm^{-1} (due to the C-O asymmetric stretching) and 864 cm^{-1} (due to the out-of-plane vibrations) in tested NCAL cathodes (Fig. 2B). Furthermore, the out-of-plane vibrations of CO_3^{2-} in the NCAL cathode with terpineol are remarkably stronger than that without terpineol after the cell test of 30 min, proving the formation of Li_2CO_3 from the reaction between NCAL and terpineol. The infrared (IR) carbonate peak of the NCAL cathode with terpineol decreased after a 2-h cell test, which was due to the diffusion of carbonates to the electrolyte that was confirmed by the elemental analyses of the cell disk (see following discussions). Although the X-ray diffraction (XRD) patterns
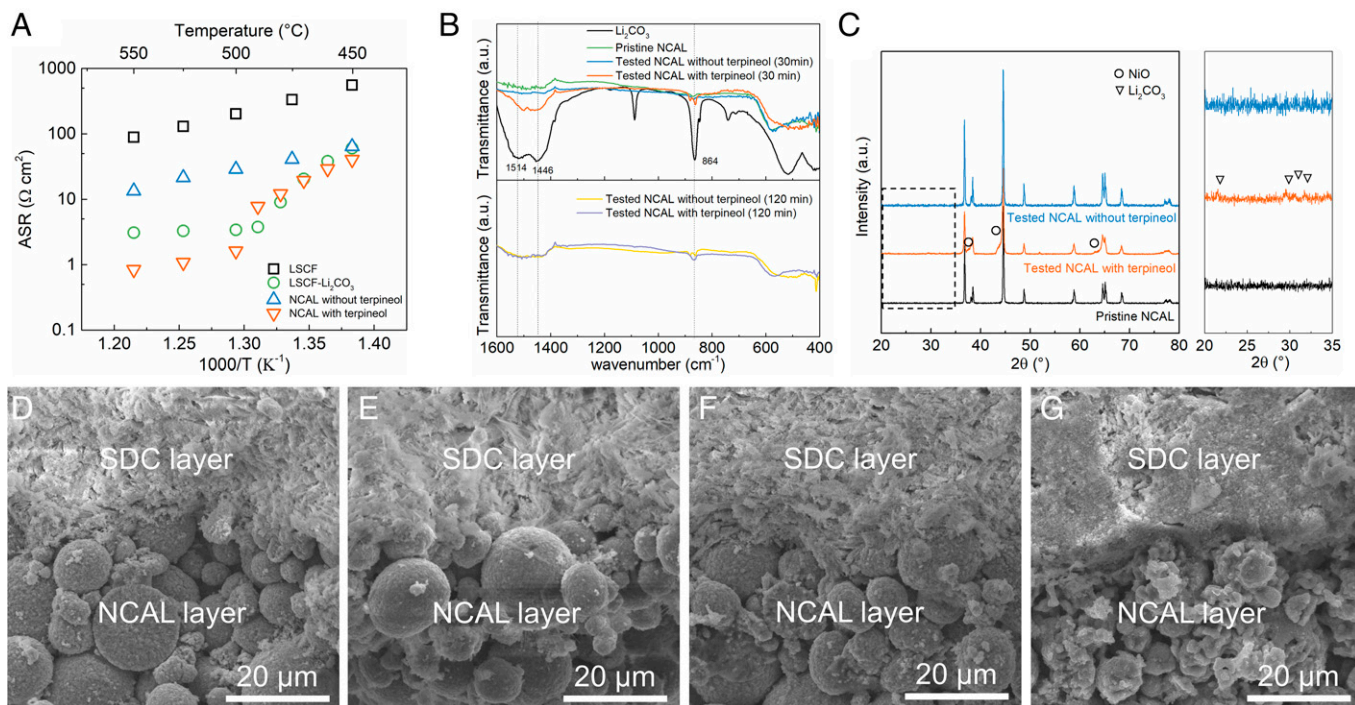
Fig. 2. Characterization of in situ generated Li_2CO_3 from NCAL. (A) Temperature dependence of the polarization resistances of different cathodes in air. (B) FTIR spectra for the NCAL electrodes. (C) XRD spectra for the NCAL electrodes. (D and E) Cross-sectional SEM image of the SDC electrolyte/NCAL cathode interface for the cell without terpineol in NCAL (D) before and (E) after cell test. (F and G) Cross-sectional SEM image of the SDC electrolyte/NCAL cathode interface of the cell with terpineol in NCAL (F) before and (G) after cell test. (Cell-test conditions: 550 °C for 2 h.)

showed that NCAL almost retained its original crystal structure after a 2-h cell test (under air atmosphere), diffraction peaks of Li_2CO_3 [Joint Committee on Powder Diffraction Standards (JCPDS), 22-1141] and NiO (JCPDS 11-2340) were detected for the NCAL cathode with terpineol, but not for that without terpineol (Fig. 2C). This further supports the Li_2CO_3 formation from the reaction between some NCAL and terpineol (Eq. **3**), but the crystal structure of most NCAL remained. The XRD peaks of produced CoO would overlap with those of NiO, because CoO and NiO have a similar crystal structure to form a solid solution (17). $LiAlO_2$, which is usually formed in NCAL decomposition (18), is too little to be detected by XRD. The microstructures of the NCAL cathode and its interface with SDC electrolyte were evaluated by scanning electron microscopy (SEM). The NCAL without terpineol maintained a spherical morphology after a 2-h cell test (Fig. 2 D and E), whereas the large spherical particles of NCAL with terpineol changed to smaller ones after the cell test (Fig. 2 F and G). The terpineol also affected the NCAL/SDC interface; namely, the NCAL with terpineol showed a better NCAL/SDC contact than that without terpineol, which would be due to the in situ formed Li_2CO_3 from the reaction between NCAL and terpineol (Eq. **3**). Furthermore, Fig. 2G shows that the SDC layer became denser after the cell test because of the diffusion of in situ formed Li_2CO_3 to the SDC layer, which was confirmed by the elemental analyses (see following discussions). Therefore, the diffusion of the in situ formed Li_2CO_3 from the NCAL to the SCD layer created the well-bonded cathode–electrolyte contact, decreasing the polarization resistance of NCAL from 13.4 to 0.84 $\Omega \cdot cm^2$ at 550 °C (Fig. 2A).

A concept of CSSFC is proposed based on the above design and experimental observations. In a CSSFC, the in situ generation of molten Li_2CO_3 diffuses from the cathode to the electrolyte, which enhances the interfacial oxygen ionic conductivity and reduces the polarization and contact resistances. Such molten carbonate in the electrolyte, electrode, and electrolyte/electrode interface is the so-called superstructured carbonate. Furthermore, we fabricated the CSSFC via a simple one-step compression process. The cross-sectional microstructures of CSSFC with NCAL cathode are shown in Fig. 3A. The CSSFC comprised a porous SDC electrolyte (~760 μm), sandwiched by a porous Ni-BZCYYb anode (~630 μm) and a NCAL/Ni foam cathode layer (~430 μm). Methane was selected as representative hydrocarbon fuel to evaluate the performance of CSSFCs. As shown by the current–voltage–power (I-V-P) polarization curves (Fig. 3B), a PPD of 215 mW·cm^{-2} at 550 °C was obtained for the CSSFC with dry CH_4 fuel, which also showed a considerable PPD of 81 mW·cm^{-2} even at 475 °C. These obtained PPDs are not only higher than all reported values of electrolyte-supported LT-SOFCs, but also comparable to those of reported anode-supported LT-SOFCs and protonic ceramic fuel cells (PCFCs) fed with dry or humidified methane fuel (*SI Appendix,* Table S1).

Furthermore, the CSSFCs exhibited ultrahigh OCV values of 0.976, 1.051, 1.076, and 1.041 V at 475, 500, 525, and 550 °C, respectively, which surpass all reported OCV values of conventional LT-SOFCs fed with dry CH_4 (Fig. 3C). The OCV of doped ceria electrolytes is often limited by internal short-circuit issues due to partial reduction of Ce^{4+} to Ce^{3+} in the reducing atmosphere (19, 20). However, the unprecedented high OCV indicates that the current leakage loss was almost totally suppressed in the CSSFC, which may be ascribed to the following reasons: the formation of an electronic blocking layer between Ni-BZCYYb and SDC electrolytes (7, 21) and relatively lower electronic conductivity of SDC at lower operation temperature (~500 °C) (22, 23). The CSSFCs being free from
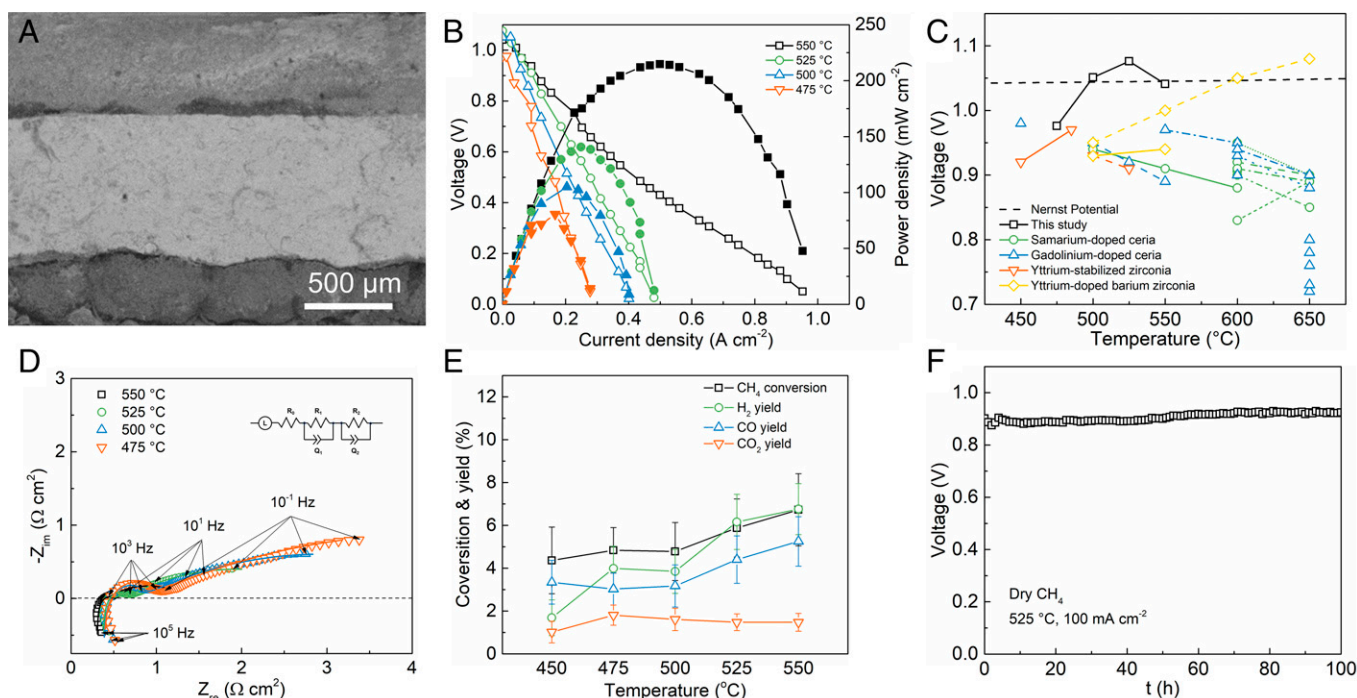

Fig. 3. Characterization and performance of CSSFC. (A) Cross-sectional SEM image of the CSSFC. (B) I-V and I-P curves of the CSSFC under CH_4 at different temperatures. (C) The measured OCVs of CSSFC in comparison with the recent reported conventional LT-SOFCs with different electrolytes fed with dry CH_4. Theoretical OCV was also estimated as the full oxidation of CH_4 ($CH_4 + 2O_2 \rightarrow CO_2 + 2H_2O$ [g]). (D) Impedance spectra of Nyquist plots of the CSSFC using CH_4 as fuel and air as oxidant at a temperature range of 475 to 550 °C. *Inset* is the equivalent circuit. (E) The methane conversion and yields of products of the CSSFCs with 100% dry CH_4 flow (~50 mL·min^{-1}) fed to the anode. (F) Durability test for CSSFC fueled with 100% dry CH_4 at 525 °C and a constant current load of 0.1 A·cm^{-2}.

current leakage loss allows them to operate with higher energy conversion efficiency. Furthermore, the ultrahigh OCV also excludes the existence of gas leakage under operation. This was further confirmed by gas chromatography (GC) analysis (*SI Appendix*, Fig. S3). When pure H_2, CH_4, and air flows were introduced into the anode or cathode of the cell without operation, significant gas permeation was observed, revealing the porous structure of the cell. In contrast, almost no gas permeation was detected during the operation (*SI Appendix*, Fig. S3B), because the in situ formed carbonate diffused into the porous electrolyte and thus plugged its microchannels (*SI Appendix*, Fig. S4A). The carbonate on the surface of SDC was confirmed by FTIR; namely, the carbonate IR absorption band was observed after 2-h operation (*SI Appendix*, Fig. S4B). The existence of molten carbonate in the SDC was also demonstrated by DSC spectrum and XRD (*SI Appendix*, Fig. S4 *C and D*). Li_2CO_3 in the SDC electrolyte was further confirmed by inductively coupled plasma (ICP) element analysis; namely, 2.11 wt% Li was determined in the electrolyte. Moreover, 0.76 wt% Li was detected in the Ni-BZCYYb anode by ICP analysis, revealing the further diffusion of Li_2CO_3 to the anode.

Fig. 3D and *SI Appendix*, Fig. S5 display the Nyquist diagrams and Bode plots of CSSFC under the CH_4/air condition and the fitting results of the equivalent circuit of $LR_o(R_1Q_1)(R_2Q_2)$ are listed in *SI Appendix*, Table S2. The terms R_o, R_1, and R_2 represent ohmic resistance and polarization resistance (sum of R_1 and R_2), while L is the high-frequency inductive component and Q the constant phase element (24, 25). The intermediate-frequency arc (R_1Q_1) is due to the ionic charge transfer at the electrode/electrolyte interface $(C_1 \sim 10^{-5}$ $F \cdot cm^{-2})$, while the low-frequency arc (R_2Q_2) is due to the gas adsorption and diffusion processes $(C_2 \sim 10^{-1}$ $F \cdot cm^{-2})$ (26, 27). The ionic conductivities of the porous SDC electrolytes can be derived from the ohmic resistance (R_o) of these cells (26, 27). The porous SDC electrolyte exhibits an ultrahigh ionic conductivity of 0.17 $S \cdot cm^{-1}$ at 550 °C. The activation energy of porous SDC electrolyte (0.31 eV) is significantly lower than the reported

values for sintered SDC pellets between ~0.65 and ~0.9 eV (28, 29). The high ionic conductivity and low activation energy of the porous SDC electrolyte can be attributed to the surface (or interfacial) ion transfer. The methane conversion and yields of products are shown in Fig. 3E. The main products are H_2 and CO, which are syngases that are an important feedstock for the synthesis of chemicals (30). This demonstrates that the CSSFC generates not only electricity but also valuable materials. It should be noted that methane conversion (about 5%) is relatively low due to low operating temperatures (Fig. 3E). However, a low-temperature operation offers many benefits, such as high theoretical efficiency, rapid thermal cycling, and low cell-fabrication cost (31, 32). Moreover, the recycling of methane fuel can increase its conversion at a low operating temperature for practical applications.

The long-term durability of the CSSFC was evaluated with dry CH_4 fuel (Fig. 3F). The CSSFC exhibited stable performance for 100 h at 525 °C. Such excellent stability was supported by SEM image and a corresponding carbon-mapping image; namely, the long-term operation did not change the morphology and surface carbon species of the Ni-BZCYYb anode (*SI Appendix*, Fig. S6). The coking resistance was further confirmed by thermogravimetric analysis (TGA) (*SI Appendix*, Fig. S7A). The slight mass gain (7 to 9 wt%) occurred due to the Ni oxidation, indicating no carbon deposition on the anode after 100-h cell operation. It should be noted that the transformation of the pure perovskite phase of BZCYYb to $BaCO_3$ was detected by XRD after the cell operation (*SI Appendix*, Fig. S7B). Similar phase changes of Ni-BZCYYb in the presence of CO_2 and H_2O were also observed for conventional SOFCs with dense electrolytes (33, 34). However, this crystal structure change did not cause further degradation of cell performance with increasing time. Furthermore, the CSSFC showed excellent flexibility for fuels, including ethane, syngas, CH_4-CO_2 (1:1), and pure CO (*SI Appendix*, Fig. S8), leading to good PPDs at 550 °C ranging from 116 $mW \cdot cm^{-2}$ for syngas to 158 $mW \cdot cm^{-2}$ for CO.
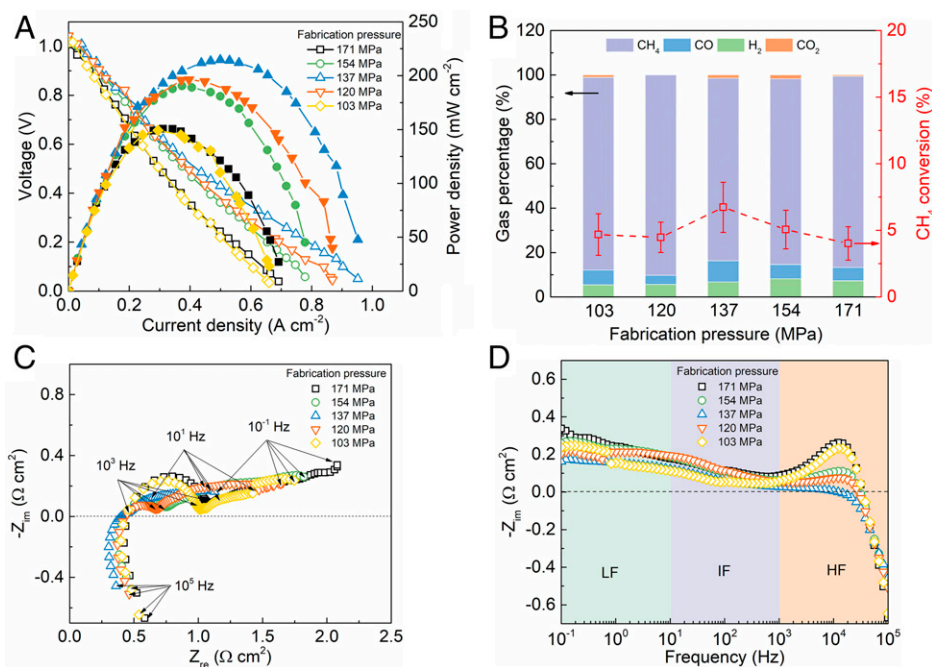
Fig. 4. Fabrication–pressure effect of CSSFC on its performance. (*A*) I-V-P performance of CSSFCs fabricated at various pressures operated on CH_4 at 550 °C. (*B*) The outlet gas composition and methane conversion under OCV at 550 °C for the cells fabricated under different pressures. (*C* and *D*) Impedance spectra of (*C*) Nyquist plots and (*D*) Bode plots for CSSFCs (fabricated at various pressures) operated on CH_4 at 550 °C.

The compressing-pressure effect of fabricating a CSSFC on its performance was also evaluated. As shown in Fig. 4*A*, the PPD of CSSFC increased from 150 to 215 mW·cm^{-2} at 550 °C with increasing fabrication pressure from 103 to 137 MPa, but further increasing pressure to 171 MPa had a negative impact with decreased PPD to 151 mW·cm^{-2}. This trend was matched with the changes in CH$_4$ conversion rate and H$_2$ production (Fig. 4*B*). The mechanism of the effects of fabrication pressure on the performances of CSSFC was further investigated by Nyquist plots (Fig. 4*C*) and Bode plots (Fig. 4*D*). The contribution of each component of ASR derived from Nyquist plots is listed in *SI Appendix*, Table S3. The ohmic resistance (R$_o$) decreased from 0.37 to 0.29 Ω·cm^2 and then increased to 0.38 Ω·cm^2 with increasing fabrication pressure from 103 to 171 MPa. A low fabrication pressure is insufficient to compact SDC particles close enough for the formation of the superstructured carbonate at the interface between the particles, and very high pressure would also diminish porosity and thus also decrease the interface between the SDC electrolyte particle and the superstructured carbonate. Similar trends were also observed for charge transfer polarization resistance (R$_1$). A decrease in fabrication pressure would create many interconnected voids, resulting in an improvement of gas diffusion and hence a decrease in low-frequency polarization resistance (R$_2$). However, further lowering the fabrication pressure could lead to poor contact between the electrolyte and electrodes, thus amplifying the polarization resistance due to the unfavorable charge transfer processes in the TPB (35, 36). These observations demonstrated that fabrication pressure of the CSSFC could have great impact on its electrochemical performance via altering the ohmic and polarization resistance.

Conclusions

We demonstrated a different type of fuel cell, CSSFC, with excellent electrochemical performance and high durability at lower operational temperatures for hydrocarbon fuels. The peak power density of a CSSFC employing a porous SDC electrolyte layer and a lithium-based cathode reached 215 mW·cm^{-2} at 550 °C with dry methane fuel. Unprecedentedly high OCVs were achieved (such as 1.051 V at 500 °C and 1.041 V at 550 °C). The CSSFC can be directly operated with various hydrocarbon fuels. The CSSFC would be promising for commercial applications due to its excellent performance, easy fabrication, low cost, and fuel flexibility.

Materials and Methods

Material Synthesis. The Ni-BZCYYb was used as an anode due to its high activity, high coking resistance, and interface electron-blocking property (7, 21). The precursor powders of BZCYYb were synthesized by the solid-state reaction method (37). The stoichiometric amounts of BaCO$_3$, ZrO$_2$, CeO$_2$, Y$_2$O$_3$, and Yb$_2$O$_3$ were mixed by hand grinding in ethanol, followed by drying for 12 h and calcination at 1,100 °C in air for 10 h. The calcined powders were then ground and calcinated again at 1,100 °C for 10 h. The BZCYYb powders were well mixed with NiO in a weight ratio of 35:65, followed by prefiring at 1,000 °C in air for 2 h (37). The Ce$_{0.8}$Sm$_{0.2}$O$_{1.9}$ (SDC) powders were prepared by the carbonate coprecipitation process (29, 38). The defined compositions of Ce(NO$_3$)$_3$·6H$_2$O and Sm(NO$_3$)$_3$·6H$_2$O were well dissolved in deionized water, followed by the addition dropwise of sodium carbonate solution with the molar ratio of metal ion and carbonate ion of 1:1.5. The obtained precipitants were washed with deionized water and ethanol several times until the pH of the filtrate became neutral. The washed precursors were dried for 12 h and then calcined at 800 °C in air for 4 h.

The CSSFC was fabricated by the dry pressing process. Commercial LSCF (Fuel Cell Materials) or NCAL (NEI Corporation) powders were mixed with terpineol binder to form a slurry, which was brush painted onto Ni foam and then dried at ~60 °C for 12 h as the cathode (38, 39). The cell configuration of Ni-BZCYYb | SDC | NCAL-Ni was fabricated by uniaxial pressing under appropriate pressure to form a pellet using 0.45 g NiO-BZCYYb anode powder, 0.35 g SDC electrolyte powder, and NCAL-coated Ni foam. The single porous cell has a thickness of ~2 mm and an active area of 0.64 cm^2.

The electrolyte-supported conventional SOFC was fabricated as follows (40, 41): The dense electrolyte pellet was prepared by dry pressing SDC precursor powders at 137 MPa with subsequent calcination at 1,350 °C in air for 5 h. A slurry composed of NiO-BZCYYb powder and terpineol was brush painted on the as-synthesized dense SDC electrolyte pellet before calcinating at 1,000 °C in air for 2 h. The cathode layer of NCAL slurry was then painted on the other side of the sintered SDC pellet and finally calcinated at 950 °C in air for 2 h. The silver mesh was used as a current collector.

The symmetrical cells were fabricated by compressing and coating processes. The appropriate amount of electrolyte powders was pressed at 137 MPa followed by calcinating at 550 or 1,350 °C for 5 h. Silver paste and terpineol mixture were then printed onto both sides of the electrolyte pellets. The symmetrical cells were fired at 550 °C for 2 h in air. The symmetrical air electrode cells were fabricated in a similar way, except the silver paste was replaced by LSCF or NCAL.

Characterization. The cross-section morphology of porous and dense pellets was investigated by environmental scanning electron microscopy (ESEM) (Philips XL 40). The elemental mapping on the anode surface before and after operating on CH$_4$ was determined using an energy-dispersive X-ray spectrometer (EDS).

The crystal structures of anode and electrolyte powders before and after operation were measured by XRD (Scintag XDS-2000) with Cu Kα (λ = 1.5406 Å) radiation. The XRD patterns were collected in the 2θ range between 20° and 80° with a scanning rate of 2°·min^{-1}. The powders after stability tests were gathered by grinding the remaining material after carefully removing the cathode layer.

FTIR was carried out on a Shimadzu IRAffinity-1 spectrometer with an in situ diffuse reflection cell (DiffusIR; PIKE Technologies), which is equipped with a ZnSe window and can be heated up to 800 °C.

The differential scanning calorimetry (DSC) of the electrolytes was performed by a Netzsch DSC 404 instrument with a TASC 414/3 controller at a heating rate of 10 °C/min under argon flow.

The outlet gas composition and gas diffusion behaviors were detected by an online GC (Hewlett-Packard 5890) coupled with a thermal conductivity detector.

The Li contents in electrolyte and anode in the tested CSSFC were determined by a PerkinElmer Optima 7000DV inductively coupled plasma-optical emission spectrometer (ICP-OES). All the samples were treated with aqua regia for 3 d before the measurement.

The TGA was carried out using the Mettler Toledo TGA/SDTA851e system. The anodes before and after long-term operation were subjected to the TGA measurement with 10 mL·min^{-1} dry air gas flow in a temperature range from 25 to 800 °C at a rate of 10 °C·min^{-1}.

Electrochemical Measurement. All these single cells were thermally treated at 550 °C for 30 min before the operation and electrochemical performance tests. The NiO-BZCYYb anode was reduced to Ni-BZCYYb in H$_2$ (99.999%) for 1 h at 550 °C prior to shifting to dry CH$_4$ (99.97%). The anode side was fed with dry CH$_4$ (~50 mL·min^{-1}), while the cathode side was fed with dry air (~300 mL·min^{-1}) as oxidant. The fuel cell I-V-P characteristics were performed using an electronic load (IT8511; ITECH Electrical Co., Ltd.) with a scan rate of 0.02 A·s^{-1} in the current-voltage sweep. Furthermore, the EIS were obtained under OCV conditions using a CHI-760 electrochemical workstation (CH Instruments, Inc.) in the frequency range of 0.1 to 10^5 Hz with a voltage amplitude of 10 mV. The impedance spectra were analyzed with the ZSimpWin 3.60 software (EChem Software) to identify the electrolyte process and the electrode process. The activation energy (E_a) was calculated with the equation

$$\sigma = \frac{A}{T}\exp\left(\frac{-E_a}{kT}\right),\qquad [4]$$

where σ is the measured conductivity, T the absolute temperature, k the Boltzmann constant, and A the preexponential factor.

1. R. M. Ormerod, Solid oxide fuel cells. *Chem. Soc. Rev.* **32**, 17–28 (2003).
2. P. Boldrin, N. P. Brandon, Progress and outlook for solid oxide fuel cells for transportation applications. *Nat. Catal.* **2**, 571–577 (2019).
3. Z. Gao, L. V. Mogni, E. C. Miller, J. G. Railsback, S. A. Barnett, A perspective on low-temperature solid oxide fuel cells. *Energy Environ. Sci.* **9**, 1602–1644 (2016).
4. Y. Zhang *et al.*, Recent progress on advanced materials for solid-oxide fuel cells operating below 500 °C. *Adv. Mater.* **29**, 1700132 (2017).
5. H. R. Su, Y. H. Hu, Progress in low-temperature solid oxide fuel cells with hydrocarbon fuels. *Chem. Eng. J.* **402**, 126235 (2020).
6. W. Zhang, Y. H. Hu, Progress in proton-conducting oxides as electrolytes for low-temperature solid oxide fuel cells: From materials to devices. *Energy Sci. Eng.* **9**, 984–1011 (2021).
7. Y. Chen *et al.*, A robust fuel cell operated on nearly dry methane at 500°C enabled by synergistic thermal catalysis and electrocatalysis. *Nat. Energy* **3**, 1042–1050 (2018).
8. S. McIntosh, R. J. Gorte, Direct hydrocarbon solid oxide fuel cells. *Chem. Rev.* **104**, 4845–4865 (2004).
9. H. Näfe, Conductivity of alkali carbonates, carbonate-based composite electrolytes and IT-SOFC. *ECS J. Solid State Sci. Technol.* **3**, 14 (2013).
10. C. Ricca, A. Ringuedé, M. Cassir, C. Adamo, F. Labat, Conduction mechanisms in oxide–carbonate electrolytes for SOFC: Highlighting the role of the interface from first-principles modeling. *J. Phys. Chem. C* **122**, 10067–10077 (2018).
11. S. A. Kumar, P. Kuppusami, B. Vigneshwaran, Y.-P. Fu, Codoped ceria Ce$_{0.8}$M$_{0.1}$Gd$_{0.1}$O$_{2−\delta}$ (M = Sm^{3+}, Sr^{2+}, Ca^{2+}) and codoped ceria–Na$_2$CO$_3$ nanocomposite electrolytes for solid oxide fuel cells. *ACS Appl. Nano Mater.* **2**, 6300–6311 (2019).
12. G. Fu *et al.*, Tuning the electronic structure of NiO via Li doping for the fast oxygen evolution reaction. *Chem. Mater.* **31**, 419–428 (2018).
13. D. R. Lide, *CRC Handbook of Chemistry and Physics* (CRC Press, 2004), vol. **85**.
14. M. D. Argyle, C. H. Bartholomew, Heterogeneous catalyst deactivation and regeneration: A review. *Catalysts* **5**, 145–269 (2015).
15. D. Yang *et al.*, Electrochemical performance of a Ni$_{0.8}$Co$_{0.15}$Al$_{0.05}$LiO$_2$ cathode for a low temperature solid oxide fuel cell. *Int. J. Hydrogen Energy* **46**, 10438–10447 (2020).
16. Y. He *et al.*, Mechanism for major improvement in SOFC electrolyte conductivity when using lithium compounds as anode. *ACS Appl. Energy Mater.* **3**, 4134–4138 (2020).
17. S. Kuboon, Y. H. Hu, Study of NiO—CoO and Co$_3$O$_4$—Ni$_3$O$_4$ solid solutions in multiphase Ni—Co—O systems. *Ind. Eng. Chem. Res.* **50**, 2015–2020 (2011).
18. M. Hofmann, M. Kapuschinski, U. Guntow, G. A. Giffin, Implications of aqueous processing for high energy density cathode materials: Part II. Water-induced surface species on LiNi$_{0.8}$Co$_{0.15}$Al$_{0.05}$O$_2$. *J. Electrochem. Soc.* **167**, 140535 (2020).
19. M. Mogensen, N. M. Sammes, G. A. Tompsett, Physical, chemical and electrochemical properties of pure and doped ceria. *Solid State Ion.* **129**, 63–94 (2000).
20. Y. Ling *et al.*, Review of experimental and modelling developments for ceria-based solid oxide fuel cells free from internal short circuits. *J. Mater. Sci.* **55**, 1–23 (2019).
21. X. Wang *et al.*, Experimental and numerical studies of a bifunctional proton conducting anode of ceria-based SOFCs free from internal shorting and carbon deposition. *Electrochim. Acta* **264**, 109–118 (2018).
22. T. Matsui, M. Inaba, A. Mineshige, Z. Ogumi, Electrochemical properties of ceria-based oxides for use in intermediate-temperature SOFCs. *Solid State Ion.* **176**, 647–654 (2005).
23. B. C. Steele, Appraisal of Ce$_{1−y}$Gd$_y$O$_{2−y/2}$ electrolytes for IT-SOFC operation at 500 °C. *Solid State Ion.* **129**, 95–110 (2000).
24. C. Jin, C. Yang, H. Zheng, F. Chen, Intermediate temperature solid oxide fuel cells with Cu$_{1.3}$Mn$_{1.7}$O$_4$ internal reforming layer. *J. Power Sources* **201**, 66–71 (2012).
25. Y. Xing *et al.*, Proton shuttles in CeO$_2$/CeO$_{2−\delta}$ core–shell structure. *ACS Energy Lett.* **4**, 2601–2607 (2019).
26. S. Ricote, N. Bonanos, F. Lenrick, R. Wallenberg, LaCoO$_3$: Promising cathode material for protonic ceramic fuel cells based on a BaCe$_{0.2}$Zr$_{0.7}$Y$_{0.1}$O$_{3−\delta}$ electrolyte. *J. Power Sources* **218**, 313–319 (2012).
27. B. Han *et al.*, Ni-(Ce$_{0.8−x}$Ti$_x$)Sm$_{0.2}$O$_{2-\delta}$ anode for low temperature solid oxide fuel cells running on dry methane fuel. *J. Power Sources* **338**, 1–8 (2017).
28. M. G. Bellino, D. G. Lamas, N. E. Walsöe de Reca, Enhanced ionic conductivity in nanostructured, heavily doped ceria ceramics. *Adv. Funct. Mater.* **16**, 107–113 (2006).
29. D. Ding, B. Liu, Z. Zhu, S. Zhou, C. Xia, High reactive Ce$_{0.8}$Sm$_{0.2}$O$_{1.9}$ powders via a carbonate co-precipitation method as electrolytes for low-temperature solid oxide fuel cells. *Solid State Ion.* **179**, 896–899 (2008).
30. Y. H. Hu, E. Ruckenstein, Comment on "Dry reforming of methane by stable Ni-Mo nanocatalysts on single-crystalline MgO". *Science* **368**, eabb5459 (2020).
31. M. Mogensen, K. Kammer, Conversion of hydrocarbons in solid oxide fuel cells. *Annu. Rev. Mater. Res.* **33**, 321–331 (2003).
32. T. M. Gür, Comprehensive review of methane conversion in solid oxide fuel cells: Prospects for efficient electricity generation from natural gas. *Pror. Energy Combust. Sci.* **54**, 1–64 (2016).
33. C. Duan *et al.*, Readily processed protonic ceramic fuel cells with high performance at low temperatures. *Science* **349**, 1321–1326 (2015).
34. Y. Zhang *et al.*, Basic properties of proton conductor BaZr$_{0.1}$Ce$_{0.7}$Y$_{0.1}$Yb$_{0.1}$O$_{3−\delta}$ (BZCYYb) material. *Asia-Pac. J. Chem. Eng.* **14,** e2322 (2019).
35. G. Chen *et al.*, Advanced fuel cell based on new nanocrystalline structure Gd$_{0.1}$Ce$_{0.9}$O$_2$ electrolyte. *ACS Appl. Mater. Interfaces* **11**, 10642–10650 (2019).
36. T. Suzuki, P. Jasinski, V. Petrovsky, H. U. Anderson, F. Dogan, Performance of a porous electrolyte in single-chamber SOFCs. *J. Electrochem. Soc.* **152**, A527 (2005).
37. L. Yang *et al.*, Enhanced sulfur and coking tolerance of a mixed ion conductor for SOFCs: BaZr$_{0.1}$Ce$_{0.7}$Y$_{0.2-x}$Yb$_x$O$_{3-\delta}$. *Science* **326**, 126–129 (2009).
38. B. Zhu *et al.*, Novel fuel cell with nanocomposite functional layer designed by perovskite solar cell principle. *Nano Energy* **19**, 156–164 (2016).
39. W. Zhang *et al.*, The fuel cells studies from ionic electrolyte Ce$_{0.8}$Sm$_{0.05}$Ca$_{0.15}$O$_{2−\delta}$ to the mixture layers with semiconductor Ni$_{0.8}$Co$_{0.15}$Al$_{0.05}$LiO$_{2−\delta}$. *Int. J. Hydrogen Energy* **41**, 18761–18768 (2016).
40. G. Yang, C. Su, Y. Chen, M. O. Tadé, Z. Shao, Nano La$_{0.6}$Ca$_{0.4}$Fe$_{0.8}$Ni$_{0.2}$O$_{3−\delta}$ decorated porous doped ceria as a novel cobalt-free electrode for "symmetrical" solid oxide fuel cells. *J. Mater. Chem. A Mater. Energy Sustain.* **2**, 19526–19535 (2014).
41. B. Hua, M. Li, J. Pu, B. Chi, L. Jian, BaZr$_{0.1}$Ce$_{0.7}$Y$_{0.1}$Yb$_{0.1}$O$_{3−\delta}$ enhanced coking-free on-cell reforming for direct-methane solid oxide fuel cells. *J. Mater. Chem. A Mater. Energy Sustain.* **2**, 12576 (2014).